ACS APPLIED MATERIALS & INTERFACES

Research Article

www.acsami.org

Hydroquinone-Assisted Synthesis of Branched Au–Ag Nanoparticles with Polydopamine Coating as Highly Efficient Photothermal Agents

Jing Li,[†] Wenjing Wang,[†] Liang Zhao,[‡] Li Rong,[§] Shijie Lan,*[,§] Hongchen Sun,*[,‡] Hao Zhang,*[,†] and Bai Yang[†]

[†]State Key Laboratory of Supramolecular Structure and Materials, College of Chemistry, Jilin University, Changchun 130012, People's Republic of China

[‡]School of Stomatology, Jilin University, Changchun 130041, People's Republic of China

[§]First Hospital of Jilin University, Changchun 130021, People's Republic of China

Supporting Information

ABSTRACT: Despite the success of galvanic replacement in preparing hollow nanostructures with diversified morphologies via the replacement reaction between sacrificial metal nanoparticles (NPs) seeds and less active metal ions, limited advances are made for producing branched alloy nanostructures. In this paper, we report an extended galvanic replacement for preparing branched Au–Ag NPs with Au-rich core and Ag branches using hydroquinone (HQ) as the reductant. In the presence of HQ, the preformed Ag seeds are replaceable by Au and, in turn, supply the growth of Ag branches. By altering the feed ratio of Ag seeds, $HAuCl_4$, and HQ, the size and morphology of the NPs are tunable. Accordingly, the surface plasmon resonance absorption is tuned to near-infrared (NIR) region, making the branched NPs as potential materials in photothermal therapy. The branched NPs are further coated with polydopamine (PDA) shell via dopamine polymerization at room temperature. In comparison with bare NPs, PDA-coated branched Au–Ag (Au–Ag@PDA) NPs exhibit improved stability, biocompatibility, and photothermal performance. In vitro experiments indicate that the branched Au–Ag@PDA NPs are competitive agents for photothermal ablation of cancer cells.

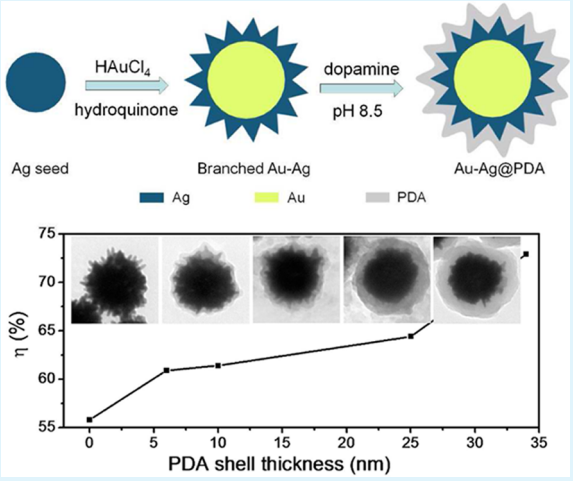

KEYWORDS: *metal nanostructures, polydopamine, nanocomposites, photothermal therapy, hydroquinone*

1. INTRODUCTION

The biomedical applications of noble metal nanomaterials have been extensively investigated over the past two decades owing to the unique plasmonic effect and the facility in morphology control, which greatly promote the creation of novel diagnostic and therapeutic technologies ranging from early cancer diagnosis to photocontrolled tumor treatment.[1−7] Among these emerging nanotechnologies, the photothermal cancer therapy by virtue of near-infrared (NIR) laser irradiation upon Au nanomaterials has attracted extraordinary interests because it permits selective treatment of tumors by minimizing the damage to normal tissues and organs.[8−11] As the kernel issue, NIR light exhibits lowered photobleaching and photodamage to organisms, thus allowing for noninvasive and deep tissue penetration.[12,13] Significant efforts are devoted to enhance the photothermal transduction efficiency in NIR region by preparing the Au nanomaterials with diversified morphologies, such as rod, shell, cage, and star.[14−18] In comparison to mostly studied nanorods, highly branched Au nanoparticles (NPs) possess larger specific surface area and easier penetration of external electromagnetic field, showing the potential as competitive photothermal agents.[19,20] However, it is less capable to adjust the plasmon resonance absorption peak of branched Au NPs to 808 nm, the most commonly employed NIR wavelength in photothermal therapy, through conventional size control, thus limiting the applicability in tumor treatment.[21] Composition control is another route to tune the properties of given nanomaterials. For example, the formation of Au–Ag alloy and core–shell structures greatly enhances the catalytic and surface-enhanced Raman activities of noble metal NPs.[22−24] So, it is reasonable to consider that the photothermal performance of branched Au NPs may be improved by preparing novel Au–Ag nanostructures.

We have tried to prepare Au–Ag core–shell NPs in aqueous media via both one-pot and Au seeded routes but failed to achieve the aimed structures due to the difficulty in avoiding

Received: March 26, 2015
Accepted: May 13, 2015
Published: May 13, 2015

DOI: 10.1021/acsami.5b02666
ACS Appl. Mater. Interfaces 2015, 7, 11613−11623

secondary nucleation. Consequently, Ag seeded route is considered for preparing branched Au−Ag NPs on the basis of galvanic replacement reaction. Galvanic replacement has been successfully applied for preparing novel nanostructures via the replacement reaction between sacrificial metal NP seeds and less active metal ions.[25,26] With respect to Ag^0 seeds and Au^{III} ions, the Au^{III} is reduced by the Ag seeds and then deposits on the surface of Ag seeds; meanwhile, the Ag^0 is oxidized to Ag^I ion and dissolves in the solution to produce pure Au or hollow Au−Ag nanostructures.[27,28] The introduction of additional reductants allow to precise control of the morphologies of the as-prepared structures. Yang et al. have demonstrated a pH-controlled preparation of hollow Ag−Au nanostructures via seeding approach.[29] Their results revealed that the species of reductants, and in particular the reducibility, are dominant for galvanic replacement reaction. Hydroxylamine is conventionally used as the selective reductant. However, because of the weak reducibility, it usually requires the elevated temperature and/or pH-control to assist the replacement reaction.[29,30] As a mild reductant, L-ascorbic acid is also employed to implement galvanic replacement. Due to the low selectivity, it only leads to the deposition of metal atoms on the template without forming branched structures.[31] Hydroquinone (HQ) is also a mild reductant, which exhibits a weak reduction potential (E_0 = −0.699 vs standard hydrogen electrode, SHE).[32] HQ has been employed to selectively reduce Ag because it is unable to initiate Ag nucleation from the Ag^I ions isolated in the solution, but it feeds the growth of existing seeds through the deposition of reduced Ag, thus avoiding secondary nucleation.[32−34] In this respect, HQ is ideal reductant for selective growth of Ag branches outside Au core.

It has been found that the structural stability of branched NPs is usually poor. Upon laser irradiation, the generated heat from the photothermal effect can melt the anisotropic nanostructures into bulk aggregation, lowering the photothermal effect in turn.[35] Coating the NPs with silica, polymer shells, or both is efficient to improve the stability.[36−39] In the case of polymer coating, polydopamine (PDA) has received significant attention, because of the unique adhesive ability, good biocompatibility, and easy bioconjugation.[40−42] Dopamine, the monomer of PDA, which contains both catechol and amine groups can spontaneously polymerize in a weak alkaline environment, which allows the polymerization under room temperature.[43,44] In particular, during polymerization, PDA can spontaneously form a coating layer on a variety of surfaces via the strong binding affinity of catechol functional groups, exhibiting the potentials as the coating for decorating nanometer- and micrometer-sized substrates.[45−48] Most recently, PDA was found possessing strong absorption in the NIR region and exhibiting excellent photothermal transduction.[49] In vivo studies confirmed that PDA has good biocompatibility and low cytotoxicity.[50] These mean that PDA will be potential coating materials for enhancing the structural stability of photothermal NPs and, simultaneously, the photothermal performance.

On the basis of the aforementioned consideration, in this work, PDA-coated branched Au−Ag (Au−Ag@PDA) NPs are prepared, which includes the preparation of branched Au−Ag NPs via Ag seeded galvanic replacement route in the presence of HQ as the reductant and the coating of PDA on branched Au−Ag NPs via dopamine room-temperature polymerization. The as-prepared Au−Ag@PDA NPs exhibit good structural stability and high photothermal transduction efficiency at 808 nm. Primary cell experiments indicate that the Au−Ag@PDA NPs possess low cytotoxicity and the capability for photothermal ablation of cancer cells.

2. EXPERIMENTAL SECTION

2.1. Materials. Analytically pure $HAuCl_4$ reagent (99.9%) was purchased from Alfa Aesar. Dopamine hydrochloride (99.0%), and tris(hydroxymethyl) aminomethans (Tris) (99.0%) were purchased from Sigma-Aldrich. Folic acid (97%) was purchased from Aladdin. Dulbecco's modified Eagle's medium with high glucose (H-DMEM), and fetal bovine serum (FBS) were purchased from Gibco. Propidium iodide (PI) was purchased from Invitrogen. Hydroquinone (HQ, 98%), sodium citrate (99.0%), $AgNO_3$ (99.8%), NaOH, and HCl were analytical grade and used as received. In all preparation, deionized water was used.

2.2. Preparation of Ag Seeds. Ag seeds were prepared according to the citrate reduction approach.[30] First, 17 mg of $AgNO_3$ was dissolved in 100 mL of deionized water and brought to boiling. Then, 2 mL of 1 w/v% sodium citrate aqueous solution was added into the $AgNO_3$ solution, and kept on boiling for 1 h. The color of the as-prepared Ag seed solution was greenish yellow. The concentration is 1 mM, referring to Ag atoms.

2.3. Preparation of Au−Ag NPs with Ag Branches. The preparation of branched Au−Ag NPs was operated under room temperature using sacrificial Ag seeds, $HAuCl_4$ aqueous solution, and the reductant of HQ. In a typical synthesis, 100 μL of 100 mM $HAuCl_4$ aqueous solution and 1 mL of 1 mM Ag seeds aqueous solution were added into 10 mL deionized water, and stirred for 2 min. The color of the solution turned from light yellow to light purple. Under vigorous stirring, 1 mL 30 mM HQ aqueous solution was added into the reaction system and maintained for 30 min to produce the branched Au−Ag NPs. The color of the solution finally turned into dark blue.

2.4. Preparation of PDA-Coated Branched Au−Ag NPs. To synthesize Au−Ag@PDA NPs, we added 12 mL of Tris-buffer into the as-prepared branched Au−Ag NPs solution and adjusted to pH 8.5, followed by adding different volume of 30 mM dopamine solution. The reaction mixture was incubated at room temperature for 3 h with the solution color gradually turning black, indicating the polymerization of dopamine. The self-polymerized dopamine in the solution was discarded by centrifugation at 6000 rpm for 5 min twice, and the Au−Ag@PDA NPs were obtained.

2.5. Cell Culture. Human cervix epithelial carcinoma cells (Hela cells) were cultured in DMEM, supplemented with 10% FBS, 100 μg/mL streptomycin, and 100 U/mL penicillin. Cells were incubated at 37 °C in humidified 5% CO_2 atmosphere. Cells were split using trypsin/EDTA medium when almost confluent.

2.6. Cytotoxicity Assay. The in vitro cytotoxicity tests were evaluated in 96-well culture plates. The Au−Ag@PDA NPs were foremost diluted to specific concentration using H-DMEM medium with 10% FBS. Cells were seeded in 96-well plates at an initial density of 3×10^3 cells/well in 0.2 mL of growth medium and incubated for 24 h prior to the addition of Au−Ag@PDA NPs. After the cellular supernatant was discarded, the cells were incubated in 200 μL different concentrations of Au−Ag@PDA NPs at 37 °C for 24 h. Standard methyl thiazolyl tetrazolium (MTT) assay was used to analyze the cell viability. The Au−Ag@PDA NPs in each concentration were assayed in five wells, and the assay was repeated three times.

2.7. Photothermal Ablation. The Hela cells were seeded in 96-well plates at an initial density of 3×10^3 cells/well in 0.2 mL growth medium and incubated for 24 h prior to the addition of Au−Ag@PDA NPs. After the cellular supernatant was discarded, the cells were incubated in 200 μL of Au−Ag@PDA NPs with specific concentrations at 37 °C for 2 h. The samples were irradiated with an 808 nm NIR laser with different laser power density for 10 min. The plates were analyzed for cell viability using MTT assay. Each laser power density was assayed in five wells and repeated three times.

2.8. Apoptosis Staining. The Hela cells were seeded at 1.0×10^5 cells/well in a 12-well flat-bottomed tissue culture plate and incubated

DOI: 10.1021/acsami.5b02666
ACS Appl. Mater. Interfaces 2015, 7, 11613−11623

for 24 h. After the cellular supernatant was discarded, the cells were incubated in 1 mL of culture medium with different concentration of Au−Ag@PDA NPs for 2 h. The samples were irradiated by an 808 nm NIR laser with different power density for 10 min. The Hela cells were cultured for 30 min and stained with 0.05 mg/mL PI.

2.9. Characterization. UV−visible absorption spectra were measured using a Shimadzu 3600 UV−vis−NIR spectrophotometer at room temperature under ambient conditions. Transmission electron microscopy (TEM) was obtained using a Hitachi H-800 electron microscope at an acceleration voltage of 200 kV with a CCD camera. High-resolution TEM (HRTEM) imaging was operated by a JEM-2100F electron microscope at 300 kV. HAADF-STEM-EDS mapping was implemented by a FEI Tecnai F20 transmission electron microscope at 200 kV. X-ray powder diffraction (XRD) investigation was measured by using Siemens D5005 diffractometer. Fourier-transform infrared (FTIR) spectra were obtained by Avatar, Nicolet. Dynamic light scattering (DLS) measurements were measured using a Zetasizer NanoZS (Malvern Instruments). Bright field and fluorescent images of Hela cells were operated by an Olympus IX51 inverted fluorescence microscope.

3. RESULTS AND DISCUSSION

3.1. HQ-Assisted Preparation of Branched Au−Ag NPs. The preparation of branched Au−Ag NPs involves the preparation of Ag seeds and subsequent galvanic replacement reaction between the seeds with $HAuCl_4$. The presence of HQ as reductant facilitates the formation of branched structures (Figure 1). In the experiments, the Ag seeds with the diameter about 50−60 nm are foremost prepared according to a typical citrate reduction method in boiling water (Figure S1, Supporting Information). After mixing with $HAuCl_4$, the galvanic replacement reaction is generated because the standard reduction potential of Au^{III}/Au^0 (1.003 V vs SHE) is higher than that of Ag^I/Ag^0 (0.799 V vs SHE).[27,32] As a result, Ag seeds are etched and oxidized into Ag^I ions. Meanwhile, Au^{III} is reduced into Au^0 and deposits on the residual Ag seeds (eq 1 and Figure S2, Supporting Information). In addition, HQ is capable to reduce excessive Au^{III} and the released Ag^I ions (eqs 2 and 3). The deposition of them on the seeds supplies the further growth of branched structures. Note that HQ is a mild reductant. The weak reduction potential (E_0= −0.699 vs SHE) avoids the secondary nucleation,[32] the main challenge in preparation branched metal nanostructures.

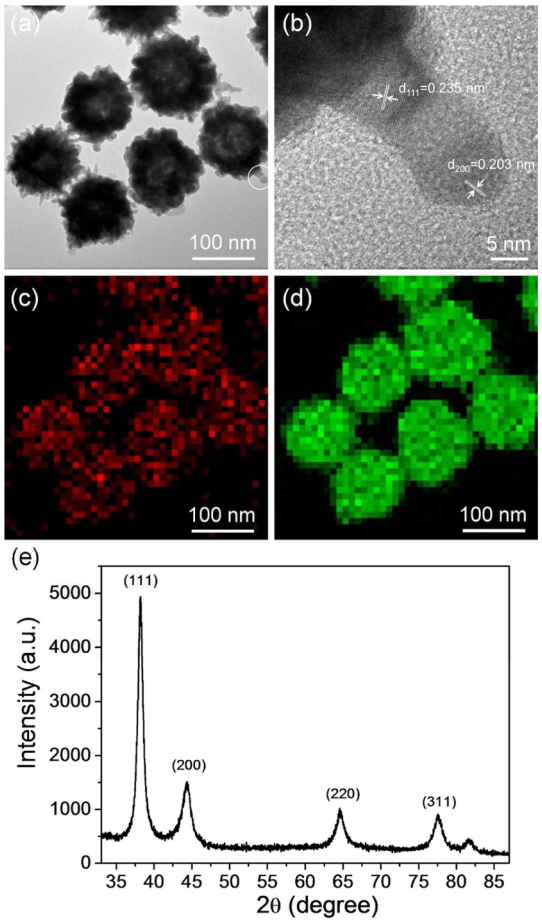

Figure 1. (a) TEM image of branched Au−Ag NPs. (b) HRTEM image of one branch of the NPs. HAADF-STEM-EDS mapping images of (c) Ag and (d) Au elements. (e) XRD pattern.

$$3Ag^0 + Au^{III} \rightarrow 3Ag^I + Au^0 \quad (1)$$

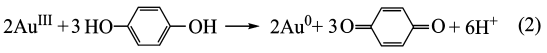

(2)

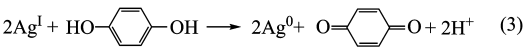

(3)

Besides the light contrast of the branches under TEM, the HRTEM image clearly indicates the interplanar distances of Ag (111) and (200) lattice planes, confirming the branches are composed of Ag (Figure 1a,b).[51] As revealed by HAADF-STEM-EDS elemental mapping images (Figure 1c,d), Ag element mainly distributes on NP surface, while a small amount of Ag also exists in the NPs. This means that the Ag seeds are not fully etched by Au^{III} during galvanic replacement (Figure S2, Supporting Information). XRD pattern exhibits the cubic structure of branched Au−Ag NPs, represented by the 2θ degrees at 38.1, 44.4, 64.6, and 77.6° of (111), (200), (220), and (311) planes (Figure 1e).[51] It should be mentioned that a strong (111) diffraction peak is observed, implying that the formation of branched NPs may occur through the rapid deposition of Au and/or Ag atoms on (111) planes. HRTEM observation confirms this speculation, which exhibits the (111) planes parallel to NP surface (Figure 1b).[26,51]

The effect of HQ on the formation of branched Au−Ag NPs is studied by altering the feed amount of HQ, while the amount of $HAuCl_4$ and Ag seeds are fixed at 100 and 1000 μL (Figure 2). When 100 μL 30 mM HQ is added, no branched structure is generated, due to the insufficient reducibility of the reaction system (Figure 2a). Namely, Au^{III}, Ag^I, or both is partially reduced to Au^0, Ag^0, or both, which fails to supply the growth of branches. As the amount of HQ is increased to 200 μL, incomplete branched NPs are observed, and some hollow spheres still exist (Figure 2b). These structures indicate the plasmon resonance (SPR) absorption peak around 600 nm (Figure 2e). When the amount of HQ reaches 500 μL, perfect branched NPs are obtained (Figure 2c), because the reducibility of the reaction system is strong enough to supply the growth of branches. This leads to the shift of SPR peak near 750 nm (Figure 2e). With the addition of 1000 μL HQ, uniform branched Au−Ag NPs with the diameter of 135 nm are achieved, while the SPR peak shifts to 800 nm (Figure 2d and e), consisting with the wavelength of mostly applied 808 nm laser in photothermal therapy.[12,35,41] These results confirm the role of HQ as reductant, which promotes the stepwise reduction of Au^{III} and Ag^I for supplying the growth of branched NPs.

DOI: 10.1021/acsami.5b02666
ACS Appl. Mater. Interfaces 2015, 7, 11613−11623

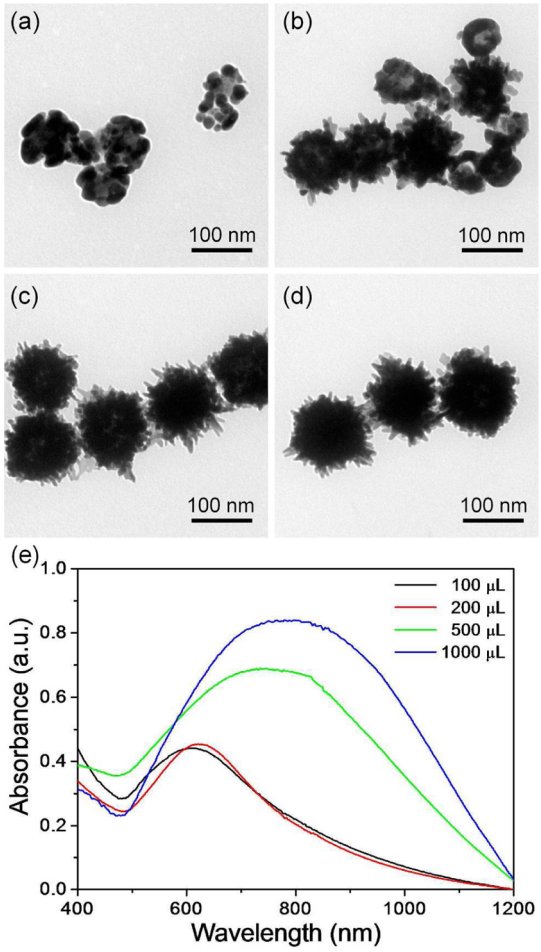

Figure 2. TEM images of Au−Ag NPs that are prepared through the addition of (a) 100, (b) 200, (c) 500, and (d) 1000 μL of 30 mM HQ aqueous solution. (e) UV−vis spectra of the NPs. The amount of $HAuCl_4$ and Ag seeds is fixed at 100 μL and 1 mL, respectively. The concentration of $HAuCl_4$ and Ag seeds solution is 100 mM and 1 mM, respectively.

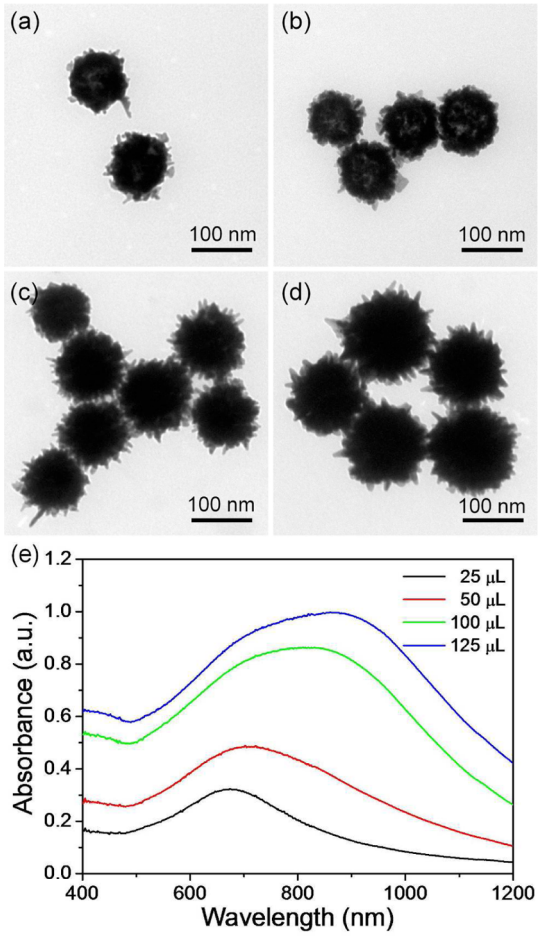

Figure 3. TEM images of branched Au−Ag NPs that are prepared through the addition of (a) 25, (b) 50, (c) 100, and (d) 125 μL of 100 mM $HAuCl_4$ aqueous solution. (e) UV−vis spectra of the NPs. Both the Ag seeds and HQ are fixed at 1000 μL. The concentration of HQ and Ag seeds solution is 30 mM and 1 mM, respectively.

The proposed formation process of branched Au−Ag NPs is further proved by altering the feed amount of $HAuCl_4$, which is the source of Au^{III} (Figure 3). The branched NPs are not well formed with the addition of 25 and 50 μL $HAuCl_4$. The Ag branches are not sharp (Figure 3a,b). This is attributed to the poor galvanic replacement of Ag seeds with insufficient Au^{III}.[27,28,31] Consequently, the oxidized Ag is insufficient for supplying the growth of sharp branches. Despite the size increase and spectral redshift, the SPR peak only shifts from 670 to 700 nm under low Au^{III} amount (Figure 3a, b and e). With the addition of 100 μL $HAuCl_4$, branched Au−Ag NPs with more than 10 sharp branches are observed (Figure 3c). The number of sharp branches further increases as $HAuCl_4$ is increased to 125 μL, accompanied by an obvious size increment (Figure 3d). Meanwhile, SPR peak shifts to 900 nm (Figure 3e). These results are consistent with our consideration that the formation of branched Au−Ag NPs involves the galvanic replacement of Ag seeds with Au^{III}. The oxidized Ag, in turn, supplies the growth of Ag branches. At a high amount of Au^{III}, a mass of Ag^I is released from the Ag seeds and finally reduced to Ag^0 by HQ. The high selective reduction of HQ avoids the secondary nucleation, leading to the rapid deposition of Ag^0 on the higher energy (111) facets of seeds.[51] Thus, branched NPs are produced.

The amount of Ag seeds is important for tuning the size of branched NPs (Figure 4). As the amount of Ag seeds increases from 100 to 1000 μL, NP diameter decreased from 290 to 135 nm. Accordingly, the SPR peak shifts from 1000 to 800 nm. Obviously, the increase of seeds decreases the amount of Au^{III} for each seed. As a result, the formation of smaller NPs is favored. Nevertheless, the as-prepared NPs preserve the morphology with branched structures, which supports the consideration that the growth of branches are supplied by the released Ag from the original Ag seeds rather than Au in the solution. To exclude the effect of citrate remaining in Ag seeds solution, we further prepared Au−Ag NPs from the Ag seeds with the removal of residual citrate. As shown in Figure S3a (Supporting Information), branched NPs still form. Furthermore, the Ag seeds that are prepared using $NaBH_4$ reducing rather than citrate are also employed for preparing Au−Ag NPs. Despite the absence of citrate, branched NPs are also produced (Figure S3b, Supporting Information). These results firmly prove that citrate does not contribute to the formation of branched nanostructures, whereas HQ is the key.

In all, the branched Au−Ag NPs are synthesized through the galvanic replacement reaction in the presence of HQ, which facilitates the formation of branched nanostructures. Because the standard reduction potential of Au^{III}/Au^0 is higher than that of Ag^I/Ag^0, the Ag seeds are oxidized into Ag^I ions by $HAuCl_4$,

DOI: 10.1021/acsami.5b02666
ACS Appl. Mater. Interfaces 2015, 7, 11613−11623

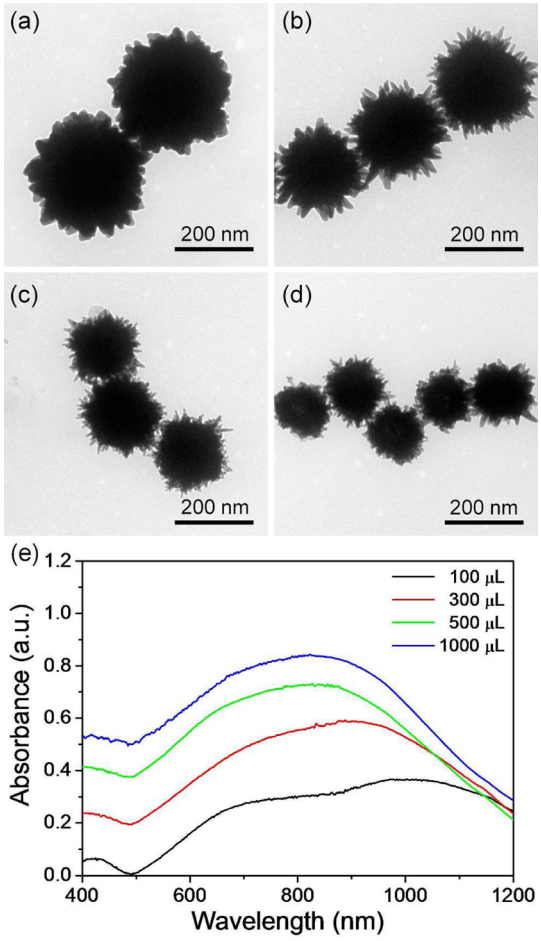

Figure 4. TEM images of branched Au−Ag NPs that are prepared through the addition of (a) 100, (b) 300, (c) 500, and (d) 1000 μL of Ag seeds aqueous solution. (e) UV−vis spectra of the NPs. The amount of $HAuCl_4$ and HQ is fixed at 100 μL and 1 mL. The concentration of HQ and $HAuCl_4$ solution is 30 and 100 mM, respectively.

and meanwhile, $HAuCl_4$ is reduced into Au^0. In addition, HQ is a mild reductant, which exhibits a weak reduction potential. Consequently, HQ is unable to reduce isolated Au^{III} ions and Ag^I ions, but is able to reduce them on the preformed seeds, thus avoiding the secondary nucleation. Moreover, because the standard reduction potential of Au^{III}/Au^0 is higher than that of Ag^I/Ag^0, the excessive Au^{III} ions are first reduced into Au^0 by HQ and deposit on the surface of the seeds. Subsequently, the released Ag^I ions are reduced into Ag^0. As HQ concentration is high enough, the deposition rate of Ag^0 on higher energy facets is faster than on lower ones, thus producing Ag branches.

3.2. PDA-Coated Branched Au−Ag NPs. Dopamine is chosen as the monomer to form polymer shell on branched Au−Ag NPs because the spontaneous polymerization in alkaline aqueous solution under room temperature is helpful to preserve the branched structure. One of the accepted mechanisms of dopamine polymerization is similar to melanin biosynthesis pathways.[52−54] In this context, the oxygen dissolved in the alkaline solution oxidizes dopamine to dopaminequinone. Then, dopaminequinone is oxidized to leucodopaminechrome through intramolecular cyclization and further oxidized to dopaminechrome. The isomerization of dopaminechrome generates 5,6-dihydroxyindole (Scheme S1, Supporting Information). The further polymerization leads to covalently bonded oligomers and/or heterogeneous aggregates. Because of the strong binding affinity of catechol functional groups, the obtained PDA can adsorb on a variety of surfaces, including noble metal NPs. In our experiments, the branched Au−Ag NPs with 135 nm in diameter are used as the core NPs for coating PDA shell. First, 12 mL of Tris-buffer solution is added into the branched NPs solution, and the pH is adjusted to 8.5. Then, a specific amount of 30 mM dopamine aqueous solution is added to perform polymerization. The color of the solution gradually turns dark, indicating the polymerization of dopamine.[49] The reaction mixtures are incubated at room temperature for 3 h and then centrifuged twice to remove the supernatant. The color of the supernatant is also black, indicating a portion of dopamine self-polymerization in the solution without coating on NPs (Figure S4a, Supporting Information). Figure 5 shows the TEM images of the as-prepared Au−Ag@PDA NPs. Under TEM, the polymer shell is clearly observed, and the branched structures are well preserved. FTIR spectrum further proves that the shell is PDA (Figure S5, Supporting Information). Note that PDA prefers to coat a single NP rather than several NPs at the same time. One possible reason is the strong electrostatic repulsion in the reaction system. The PDA coating is operated at pH 8.5. Under this basic condition, both dopamine monomers and the

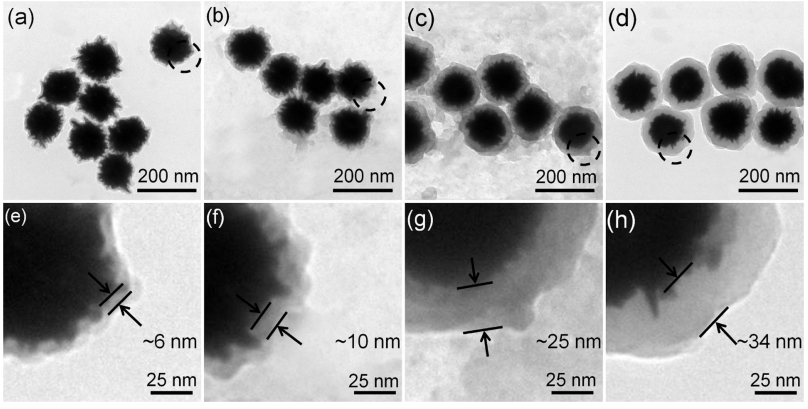

Figure 5. TEM images of branched Au−Ag@PDA NPs that are prepared through the addition of (a and e) 100, (b and f) 200, (c and g) 400, and (d and h) 600 μL of 30 mM dopamine aqueous solution to the as-prepared branched Au−Ag NPs. The pH of solution is fixed at 8.5 with the addition of Tris-buffer and NaOH adjustment.

DOI: 10.1021/acsami.5b02666
ACS Appl. Mater. Interfaces 2015, 7, 11613−11623

primarily formed PDA-coated NPs are negatively charged. According to the Debye–Hückel theory, the coating of a single NP is favored under this condition.[55]

The thickness of PDA shell is controlled by altering the feed amount of dopamine. As increasing dopamine from 100 to 600 μL, the shell thickness gradually increases from 6 to 34 nm (Figure 5a–h). Accordingly, the UV–vis absorption spectra show strong red shift (Figure 6). It is known that PDA has

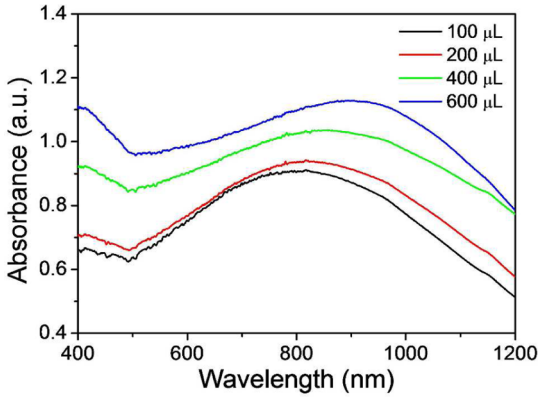

Figure 6. UV–vis spectra of branched Au–Ag@PDA NPs that are prepared through the addition of 100, 200, 400, and 600 μL of 30 mM dopamine aqueous solution to the as-prepared branched Au–Ag NPs. The pH of the solution is fixed at 8.5 with the addition of Tris-buffer and NaOH adjustment.

obvious absorbance at NIR region (Figure S4b, Supporting Information). So, the red shift of Au–Ag@PDA NPs absorption is mainly attributed to the absorption of PDA shell. Moreover, optical plasmon resonance is associated with the collective oscillation of the conduction electron confined in the NPs.[56,57] The surface plasmons can be excited by incident light in a process that depends on the dielectric constant of the materials at metal surface.[58,59] According to the Mie theory, the electron vibration is confined in a small space as they are coated with a shell, which shortens the extent of electron vibration and leads to the red shift of plasmon resonance absorption.[37,38,60–62] The red shift of the plasmon relates to the thickness of the coating materials, which can be expressed as eq 4:[63]

$$\Delta\lambda = m\Delta n[1 - \exp(-2d/l_d)] \quad (4)$$

where m is the refractive-index response of the NPs, Δn is the change in refractive-index induced by the adsorbate, d is the effective adsorbate layer thickness, and l_d is the characteristic EM-field-decay length (approximated as an exponential decay). In the current system, m = 703 nm/refractive index units,[64] $\Delta n = n_{PDA} - n_{water}$ = 1.6–1.33, and l_d = 200 nm. For the PDA thickness of 6, 10, and 25 nm (Figure 5a–c), the calculated wavelength shift is 11, 17, and 42 nm, respectively, matching well with the shift of absorption spectra (Figure 6). However, when the PDA thickness reaches 35 nm, the calculated wavelength shift is 56 nm, much less than the actual shift of 117 nm. It may be attributed to the strong absorption of PDA in the NIR region. Namely, the spectral red shift is not only led from the change of dielectric environment on the NPs surface, but also from the strong absorption of PDA in the NIR region.

The pH of the solution greatly influences the coating of PDA on the branched NPs by altering the equilibrium of dopamine polymerization on NPs and self-polymerization in solution. As increasing the pH from 7.5 to 9.0, the color of the solution becomes darker, indicting the formation of more PDA. After centrifugation, the color of supernatant with the pH of 9.0 is darkest, indicating the tendency of self-polymerization in the solution rather than on NPs surface. Under TEM, the thickness of PDA shell decreases from 23, 15, 10, to 8 nm with pH increment (Figure S6, Supporting Information). A clear blue shift of the UV–vis absorption spectra is also observed as the pH increases from 7.5 to 9.0 (Figure 5e), which is consistent with the TEM observation. These results clearly indicate that competitive polymerization of dopamine on NPs and in solution are determined by the initial pH of solution. In this context, despite high pH promoting the initial polymerization of dopamine without selectivity, more PDA particles form in the solution because the number of branched Au–Ag NPs is fixed. In turn, these PDA particles act as the seeds for adsorption and subsequent polymerization of dopamine in the solution. As a result, more PDA forms in the solution after polymerization.

3.3. Stability of Branched Au–Ag@PDA NPs. The PDA coating greatly improves the structural stability of branched Au–Ag NPs. As shown in Figure S7 (Supporting Information), the thermal stability of the branched Au–Ag NPs with and without PDA coating is compared by incubating in 50 °C water. No obvious spectral shift is found for Au–Ag@PDA NPs after 6 h incubation (Figure S7b, Supporting Information). In comparison, clear intensity decrease and blue shift of the absorption spectra are observed for bare NPs (Figure S7a, Supporting Information). The photothermal stability is further compared by irradiating Au–Ag NPs and Au–Ag@PDA NPs with 3 W/cm^2 808 nm NIR laser (Figure S7c,d, Supporting Information). Au–Ag@PDA NPs exhibit better stability than Au–Ag NPs. With respect to the improved stability, the Au–Ag NPs are not modified with capping ligands. So, the surface atoms are very active. During room-temperature storage, heating, or laser irradiation, they have the tendency to lose branched structures or aggregate driven by the high surface energy. PDA coating provides a protective layer, thus improving the structural stability.

For further biomedical applications, the physiological stability of branched Au–Ag NPs and Au–Ag@PDA NPs is studied by incubating in physiological saline (0.9% NaCl), phosphate buffered saline (PBS), and medium with and without 10% serum. The UV–vis absorption spectra are compared after 1 h of incubation (Figure 7). Both the Au–Ag NPs and Au–Ag@PDA NPs are stable in the medium with 10% serum, represented by a lesser change of absorption spectra. In 0.9% NaCl, the absorption spectrum of Au–Ag@PDA NPs is still unchanged, whereas the absorption intensity of Au–Ag NPs decreases by half, showing the better stability of Au–Ag@PDA NPs than Au–Ag NPs. In PBS and the medium without serum, the stability of Au–Ag@PDA NPs is also better than Au–Ag NPs (Figure 7). In the investigated range of PDA shell from 6 to 34 nm, the colloidal stability and physiological stability of Au–Ag@PDA NPs is independent of the PDA shell thickness. A 10 nm PDA shell is enough for further applications.

3.4. Photothermal Performance of Branched Au–Ag@PDA NPs. Both the branched Au–Ag NPs and Au–Ag@PDA NPs exhibit good photothermal performance. In particular, after coating Au–Ag NPs with PDA shell, the SPR peak further red shifts to NIR region, matching the 808 nm wavelength of mostly used laser in photothermal therapy. Taking the branched NPs with the diameter of 135 nm as an example, we investigated the influence of PDA shell thickness on the

DOI: 10.1021/acsami.5b02666
ACS Appl. Mater. Interfaces 2015, 7, 11613–11623

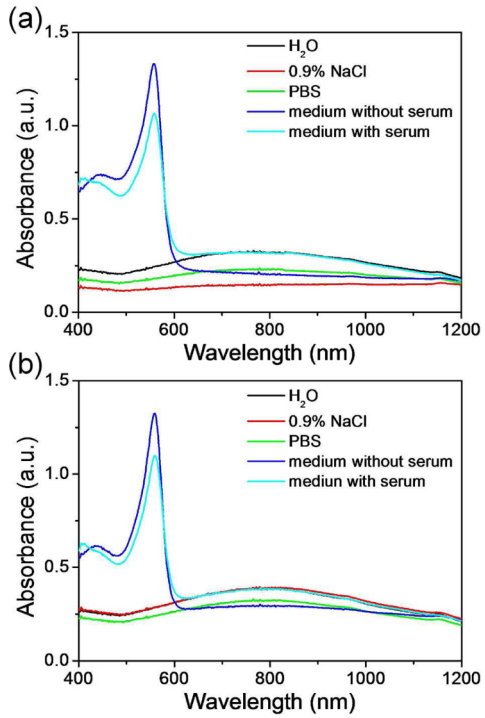

Figure 7. Comparison of the UV−vis absorption spectra of branched Au−Ag NPs (a) and Au−Ag@PDA NPs (b) after 1 h of storage at room temperature in H_2O, 0.9% NaCl, PBS, and medium with and without 10% serum.

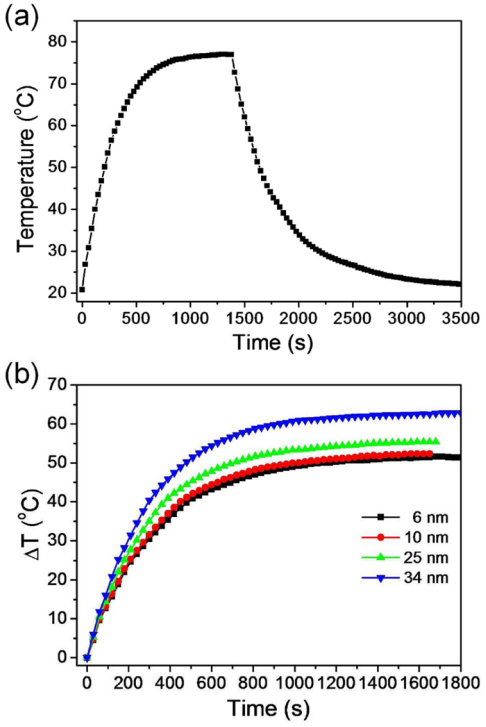

Figure 8. (a) The temporal temperature variation of the aqueous solution of 135 nm branched Au−Ag NPs. The solution is irradiated by 3 W/cm^2 808 nm laser until steady state temperature, and cooled to room temperature under ambient environment. (b) The temperature increment of branched Au−Ag@PDA NPs solution with different PDA shell thickness versus irradiation time upon 3 W/cm^2 808 nm. The core is the branched Au−Ag NPs with 135 nm in diameter. The amount of Au is fixed at 0.16 mg.

photothermal behavior. First, 2 mL of NP aqueous solution with a fixed Au amount (0.16 mg) is placed in a quartz cell. A thermoelectric thermometer is inserted into the solution to monitor the real-time temperature change. An 808 nm laser with a power density of 3 W/cm^2 is employed to irradiate the NPs solution, until steady state temperature is reached. Subsequently, the laser is shut off, and the temperature decease is monitored to determine the rate of heat transfer from the dispersion system to the environment (Figure 8a). Compared with Au−Ag NPs, the temperature increment in the presence of Au−Ag@PDA NPs is higher. The more shell thickness, the higher temperature increases (Figure 8b). This qualitatively indicates that a PDA shell is helpful to enhance the photothermal performance of branched Au−Ag NPs.

Following the method developed by Roper et al. and Hu et al.,[65,66] the photothermal transduction efficiency (η) is calculated according to eq 5.

$$\eta = \frac{hS(T_{max} - T_{surr}) - Q_{dis}}{I(1 - 10^{-A808})} \quad (5)$$

where h is heat transfer coefficient, S is the surface area of the container, and the value of hS can be obtained according to Figure S8b, Supporting Information. The T_{max} is the maximum steady-state temperature, and T_{surr} is the temperature of the environment. Q_{dis} represents the heat generated by water and quartz cell under laser irradiation, which is measured independently using a quartz cell containing 2 mL of pure water. I is the incident laser power, and A_{808} is the absorbance of the NPs at 808 nm. For the branched Au−Ag NPs with the diameter of 135 nm, η is calculated to be 55.8%, much higher than that ever reported for Au nanostars (27%), Au nanorods (21%), Au nanoshells (13%), and pure PDA NPs (40%).[35,49,67]

In addition, η gradually increases with the increase of the diameters of branched NPs and the thickness of PDA shell (Table 1 and S1). For the Au−Ag@PDA NPs with 10 nm PDA shell, the calculated η is 61.4%. The η even increases to 72.9% for the Au−Ag@PDA NPs with 34 nm PDA shell. The result is consistent with the measured temperature increment (Figure 8b), confirming that the PDA shell contributes to the enhanced photothermal performance.

Table 1. Comparison of the Photothermal Transduction Efficiency (η) of Branched Au−Ag@PDA NPs with Different PDA Thickness[a]

thickness (nm)	0	6	10	25	34
η (%)	55.8	60.9	61.4	64.4	72. 9

[a]The diameter of branched Au−Ag NPs is 135 nm.

The good photothermal performance also relates to the extinction capability of NPs because the extinction intensity is associated with the available electrons in the oscillation system. Taking 135 nm Au−Ag NPs as an example, the molar extinction coefficient (ε) is 3.23 × 10^{11} M^{-1} cm^{-1} at 808 nm. After being coated with 10 nm PDA shell, ε increases to 3.36 × 10^{11} M^{-1} cm^{-1} (Table S2 and S3, Supporting Information). The increase of ε after PDA coating is consistent with the aforementioned results that PDA shell facilitates the light harvest under irradiation, thus enhancing the photothermal performance. Note that the ε of Au−Ag NPs and Au−Ag@PDA NPs is much higher than that of Au nanorods (1.9 × 10^9 M^{-1} cm^{-1}),

DOI: 10.1021/acsami.5b02666
ACS Appl. Mater. Interfaces 2015, 7, 11613−11623

Au nanostars (3.5×10^{10} M^{-1} cm^{-1}), and Au nanoshells (2×10^{11} M^{-1} cm^{-1}).[35,67] This extinction property allows the branched Au−Ag NPs as competitive agents in photothermal applications.

3.5. In Vitro Photothermal Therapy. The photothermal applications of branched Au−Ag@PDA NPs is tested by studying the efficiency in photothermal ablation of Hela cells.

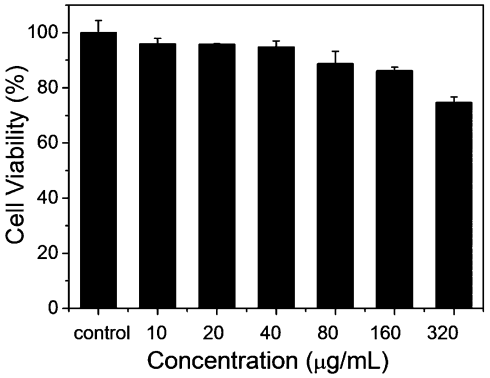

Figure 9. Cytotoxicity of branched Au−Ag@PDA NPs in Hela cells, which is revealed by the incubation of Hela cells in 100 μL culture medium with different concentrations of Au−Ag@PDA NPs for 24 h and followed by MTT assay. The thickness of PDA shell is 10 nm.

The cytotoxicity of branched Au−Ag@PDA NPs is first studied through standard MTT assay of the cell viability (Figure 9). As the concentration of Au−Ag@PDA NPs is lower than 80 μg/mL, the cell viability is more than 94.7%. Even with the concentration increased to 320 μg/mL, the viability is still 74%. The low toxicity of the Au−Ag@PDA NPs is attributed to the PDA coating, which prevents the release of toxic metal ions, organic molecules, or both. Meanwhile, PDA is biocompatible.

In the in vitro photothermal test, Hela cells are foremost incubated in the culture medium for 2 h with the presence of Au−Ag@PDA NPs, and followed by 808 nm NIR laser irradiation. After laser treatment, the cells are stained with PI, which penetrates dead cells only.[8,39] In general, the ratio of dyed cells increases with the increase of laser intensity and the dosage of Au−Ag@PDA NPs (Figure 10), which reveals the accelerated cell apoptosis under strong NIR irradiation, high dosage of NPs, or both. The influence of laser power density on the photothermal ablation is studied by combining apoptosis staining and MTT assay (Figure 10a−i). Under the power density of 0.5 W/cm^2, the cell viability in the presence of 80 μg/mL Au−Ag@PDA NPs is 57%. When the power density is increased to 1 W/cm^2, the cell viability dramatically decreases to 14% (Figure 10i). The high cell apoptosis ratio at such low power density indicates the excellent performance of Au−Ag@PDA NPs in photothermal ablation of Hela cells. A similar effect of laser power density is observed the dosage of

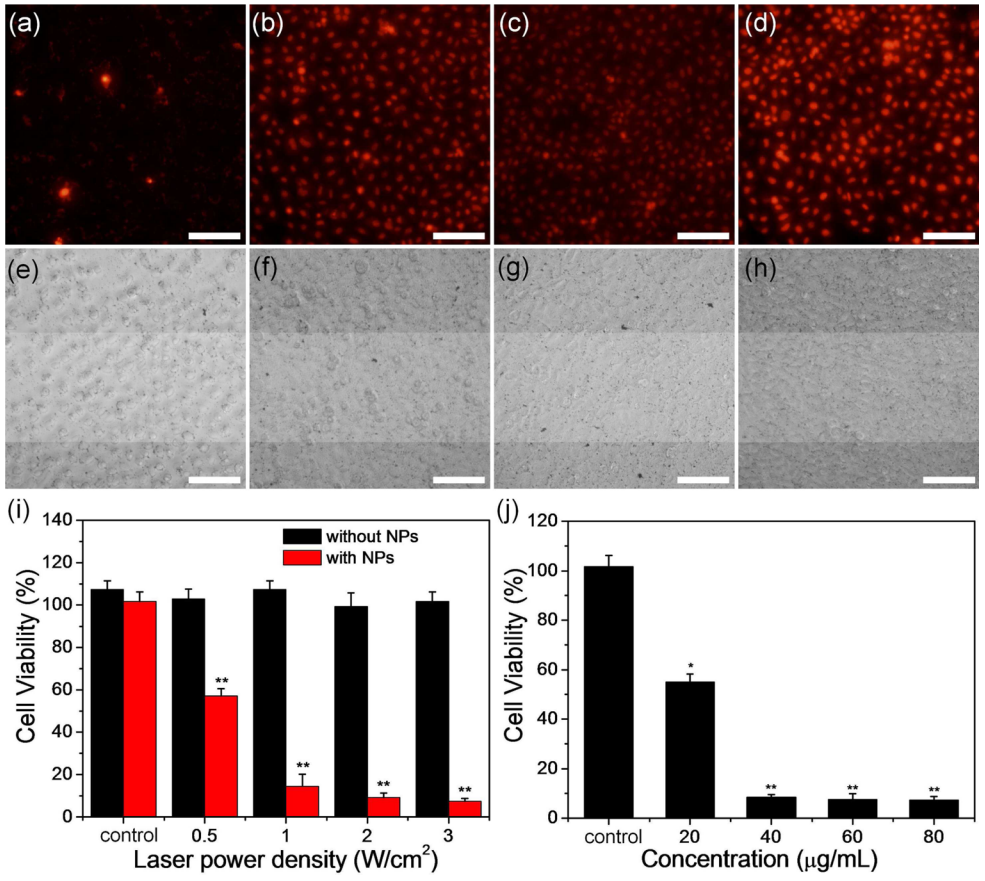

Figure 10. (a−d) Fluorescent and (e−h) bright field images of Hela cells after irradiated by an 808 nm laser with the power density of (a and e) 0.5, (b and f) 1, (c and g) 2, and (d and h) 3 W/cm^2 for 10 min. The scale bar is 100 μm. (i) Hela cell viabilities after 808 nm laser irradiation with the power density of 0.5, 1, 2, and 3 W/cm^2 for 10 min. The Hela cells are foremost incubated with 80 μg/mL branched Au−Ag@PDA NPs for 4 h. (j) Hela cell viabilities versus the concentration of Au−Ag@PDA NPs, which is studied using 808 nm laser irradiation with a power density of 2 W/cm^2 for 10 min. The thickness of the PDA shell is 10 nm. Data are shown as means ± standard error of the means, * $p < 0.05$ and ** $p < 0.01$.

DOI: 10.1021/acsami.5b02666
ACS Appl. Mater. Interfaces 2015, 7, 11613−11623

Au−Ag@PDA NPs is decreased (Figure S9a−d, Supporting Information). Moreover, upon laser irradiation, the cell viability ratio decreases significantly with the increase of Au−Ag@PDA NPs concentration. More than 67% of cells remain alive with a Au−Ag@PDA NP concentration of 20 μg/mL upon 2 W/cm^2 laser irradiation. The cell viability decreases to 9% as the concentration of Au−Ag@PDA NPs increases 40 μg/mL (Figure 10j). Under lowered laser power density, a similar tendency is also observed (Figure S9e−h, Supporting Information). Control experiment indicates that the laser irradiation in the absence of Au−Ag@PDA NPs has no influence on the viability of Hela cells. In addition, without laser irradiation, the incubation of Hela cells with Au−Ag@PDA NPs leads to negligible cell apoptosis, and almost no cells are stained by PI. These confirm that the cell apoptosis is led from the photothermal effect of branched Au−Ag@PDA NPs. In all, the aforementioned results demonstrate the excellent performance of branched Au−Ag@PDA NPs for inducing Hela cell apoptosis via photothermal protocol.

Furthermore, the bioconjugation potentials of Au−Ag@PDA NPs is tested by connecting with folic acid, which is conventionally employed for targeting cancer cells with folic acid receptors.[68] To conjugate with folic acid, Au−Ag@PDA NPs are dispersed in folic acid-contained Tris buffer (pH 8.5).[42] After 1 h of incubation at room temperature, the NPs are collected by centrifugation and washed with deionized water twice to remove unconnected folic acid. By comparing the FTIR spectra, we proved the connection with folic acid (Figure S10, Supporting Information).[69] The simplicity of conjugation with targeting molecules will promote the applications of Au−Ag@PDA NPs in selective treatment of tumor cells.

To demonstrate the difference of our materials with the existed photothermal materials, we compared the performance and toxicity of branched Au−Ag NPs with CTAB-coated Au nanorods, which are the most commonly used photothermal materials. To compare photothermal performance, we used the branched Au−Ag NPs and Au nanorods with plasmon resonance absorption peak at 800 nm (Figure S11a, Supporting Information). The mass concentration is fixed at 50 μg/mL. As irradiating 2 mL solution by 808 nm laser with a power density of 3 W/cm^2, the temperature increment of Au nanorods solution is slightly higher than that of branched Au−Ag NPs, showing the better photothermal performance (Figure S11b, Supporting Information). Nevertheless, the temperature increment of branched Au−Ag NPs is beyond 46 °C, which is high enough for photothermal therapy. In addition, the toxicity of branched Au−Ag NPs is much lower than that of CTAB-coated Au nanorods. As we know, CTAB is very toxic in biological systems. Additional purification of Au nanorods must be done before biological applications. The good photothermal performance and the low toxicity make branched Au−Ag NPs as competitive candidates for photothermal therapy.

4. CONCLUSIONS

In summary, branched Au−Ag@PDA NPs are prepared through the preparation of branched Au−Ag NPs via Ag seeded galvanic replacement route in the presence of HQ as the reductant, and the subsequent coating of PDA on NPs via dopamine room-temperature polymerization. The branched Au−Ag NPs possess strong SPR absorption in NIR region, thus showing the potential as photothermal agents. PDA coating further enhances the structural stability and biocompatibility of branched NPs. In particular, the photothermal transduction efficiency is further improved to 70% after PDA coating, much higher than other Au nanostructures and composite materials. In vitro experiments indicate that the Au−Ag@PDA NPs possess low cytotoxicity and the capability for photothermal ablation of cancer cells.

■ ASSOCIATED CONTENT

Supporting Information

Additional TEM images, HAADF-STEM-EDS mapping images, FTIR spectra, absorption spectra, fluorescent images, and method for calculating photothermal transduction efficiency. The Supporting Information is available free of charge on the ACS Publications website at DOI: 10.1021/acsami.5b02666.

■ AUTHOR INFORMATION

Corresponding Authors

* Fax: +86 431 85193423. Tel: +86 431 85159205.
* E-mail: hao_zhang@jlu.edu.cn. E-mail: hcsun@mail.jlu.edu.cn.
* E-mail: lanshijie@jlu.edu.cn.

Notes

The authors declare no competing financial interest.

■ ACKNOWLEDGMENTS

This work was supported by NSFC (51425303, 21374042, 21174051, 21221063, 81320108011, 81301650), the 973 Program of China (2014CB643503), the Natural Science Foundation of Jilin Province (20140101048JC), the Special Project from MOST of China, and the Fundamental Research Funds for the Central Universities.

■ REFERENCES

(1) Sperling, R. A.; Gil, P. R.; Zhang, F.; Zanella, M.; Parak, W. J. Biological Applications of Gold Nanoparticles. *Chem. Soc. Rev.* **2008**, *37*, 1896−1908.
(2) Cobley, C. M.; Chen, J.; Cho, E. C.; Wang, L. V.; Xia, Y. Gold Nanostructures: A Class of Multifunctional Materials for Biomedical Applications. *Chem. Soc. Rev.* **2011**, *40*, 44−56.
(3) Jain, P. K.; Huang, X.; El-Sayed, I. H.; El-Sayed, M. A. Noble Metals on the Nanoscale: Optical and Photothermal Properties and Some Applications in Imaging, Sensing, Biology, and Medicine. *Acc. Chem. Res.* **2008**, *41*, 1578−1586.
(4) Sau, T. K.; Rogach, A. L.; Jäckel, F.; Klar, T. A.; Feldmann, J. Properties and Applications of Colloidal Nonspherical Noble Metal Nanoparticles. *Adv. Mater.* **2010**, *22*, 1805−1825.
(5) Alkilany, A. M.; Lohse, S. E.; Murphy, C. J. The Gold Standard: Gold Nanoparticle Libraries to Understand the Nano-Bio Interface. *Acc. Chem. Res.* **2013**, *46*, 650−661.
(6) Saha, K.; Agasti, S. S.; Kim, C.; Li, X.; Rotello, V. M. Gold Nanoparticles in Chemical and Biological Sensing. *Chem. Rev.* **2012**, *112*, 2739−2779.
(7) Lin, J.; Wang, S.; Huang, P.; Wang, Z.; Chen, S.; Niu, G.; Li, W.; He, J.; Cui, D.; Lu, G.; Chen, X.; Nie, Z. Photosensitizer-Loaded Gold Vesicles with Strong Plasmonic Coupling Effect for Imaging-Guided Photothermal/Photodynamic Therapy. *ACS Nano* **2013**, *7*, 5320−5329.
(8) Melancon, M. P.; Zhou, M.; Li, C. Cancer Theranostics with Near-Infrared Light-Activatable Multimodal Nanoparticles. *Acc. Chem. Res.* **2011**, *44*, 947−956.
(9) Zhang, Z. J.; Wang, J.; Chen, C. Y. Near-Infrared Light-Mediated Nanoplatforms for Cancer Thermo-Chemotherapy and Optical Imaging. *Adv. Mater.* **2013**, *25*, 3869−3880.
(10) Shi, P.; Liu, Z.; Dong, K.; Ju, E.; Ren, J.; Du, Y.; Li, Z.; Qu, X. A Smart "Sense−Act−Treat" System: Combining a Ratiometric pH

DOI: 10.1021/acsami.5b02666
ACS Appl. Mater. Interfaces 2015, 7, 11613−11623

Sensor with a Near Infrared Therapeutic Gold Nanocage. *Adv. Mater.* **2014**, *26*, 6635−6641.
(11) Liu, H.; Liu, T.; Wu, X.; Li, L.; Tan, L.; Chen, D.; Tang, F. Targeting Gold Nanoshells on Silica Nanorattles: a Drug Cocktail to Fight Breast Tumors via a Single Irradiation with Near-Infrared Laser Light. *Adv. Mater.* **2012**, *24*, 755−761.
(12) Cheng, L.; Yang, K.; Chen, Q.; Liu, Z. Organic Stealth Nanoparticles for Highly Effective in Vivo Near-Infrared Photothermal Therapy of Cancer. *ACS Nano* **2012**, *6*, 5605−5613.
(13) Chen, W. R.; Adamsc, R. L.; Carubellic, R.; Nordqust, R. E. Laser-Photosensitizer Assisted Immunotherapy: A Novel Modality for Cancer Treatment. *Cancer Lett.* **1997**, *115*, 25−30.
(14) Hirsch, L. R.; Stafford, R. J.; Bankson, J. A.; Sershen, S. R.; Rivera, B.; Price, R. E.; Hazle, J. D.; Halas, N. J.; West, J. L. Nanoshell-Mediated Near-Infrared Thermal Therapy Of Tumors under Magnetic Resonance Guidance. *Proc. Natl. Acad. Sci. U.S.A.* **2003**, *23*, 13549−13554.
(15) Ke, H.; Wang, J.; Dai, Z.; Jin, Y.; Qu, E.; Xing, Z.; Guo, C.; Yue, X.; Liu, J. Gold-Nanoshelled Microcapsules: A Theranostic Agent for Ultrasound Contrast Imaging and Photothermal Therapy. *Angew. Chem., Int. Ed.* **2011**, *50*, 3017−3021.
(16) Zhang, Z.; Wang, L.; Wang, J.; Jiang, X.; Li, X.; Hu, Z.; Ji, Y.; Wu, X.; Chen, C. Mesoporous Silica-Coated Gold Nanorods as a Light-Mediated Multifunctional Theranostic Platform for Cancer Treatment. *Adv. Mater.* **2012**, *24*, 1418−1423.
(17) Glaus, C.; Laforest, R.; Zhang, Q.; Yang, M.; Gidding, M.; Welch, M. J.; Xia, Y. Gold Nanocages as Photothermal Transducers for Cancer Treatment. *Small* **2010**, *6*, 811−817.
(18) Wang, X.; Li, G.; Ding, Yu.; Sun, S. Understanding the Photothermal Effect of Gold Nanostars And Nanorods for Biomedical Applications. *RSC Adv.* **2014**, *4*, 30375−30383.
(19) Yuan, H.; Fales, A. M.; Vo-Dinh, T. TAT Peptide-Functionalized Gold Nanostars: Enhanced Intracellular Delivery and Efficient NIR Photothermal Therapy Using Ultralow Irradiance. *J. Am. Chem. Soc.* **2012**, *134*, 11358−11361.
(20) Van de Broek, B.; Devoogdt, N.; D'Hollander, A.; Gijs, H.-L.; Jans, K.; Lagae, L.; Muyldermans, S.; Maes, G.; Borghs, G. Specific Cell Targeting with Nanobody Conjugated Branched Gold Nanoparticles for Photothermal Therapy. *ACS Nano* **2011**, *5*, 4319−4328.
(21) Li, J.; Wu, J.; Zhang, X.; Liu, Y.; Zhou, D.; Sun, H. Z.; Zhang, H.; Yang, B. Controllable Synthesis of Stable Urchin-like Gold Nanoparticles Using Hydroquinone to Tune the Reactivity of Gold Chloride. *J. Phys. Chem. C* **2011**, *115*, 3630−3637.
(22) Cui, Y.; Ren, B.; Yao, J.-L.; Gu, R.-A.; Tian, Z.-Q. Synthesis of $Ag_{core}Au_{shell}$ Bimetallic Nanoparticles for Immunoassay Based on Surface-Enhanced Raman Spectroscopy. *J. Phys. Chem. B* **2006**, *110*, 4002−4006.
(23) Cheng, L.-C.; Huang, J.-H.; Chen, H. M.; Lai, T.-C.; Yang, K.-Y.; Liu, R.-S.; Hsiao, M.; Chen, C.-H.; Her, L.-J.; Tsai, D. P. Seedless, Silver-Induced Synthesis of Star-Shaped Gold/Silver Bimetallic Nanoparticles as High Efficiency Photothermal Therapy Reagent. *J. Mater. Chem.* **2012**, *22*, 2244−2253.
(24) Gu, J.; Zhang, Y.-W.; Tao, F. F. Shape Control of Bimetallic Nanocatalysts Through Well-Designed Colloidal Chemistry Approaches. *Chem. Soc. Rev.* **2012**, *41*, 8050−8065.
(25) Ridelman, Y.; Singh, G.; Popovitz-Biro, R.; Wolf, S. G.; Das, S.; Klajn, R. Metallic Nanobowls by Galvanic Replacement Reaction on Heterodimeric Nanoparticles. *Small* **2012**, *8*, 654−660.
(26) Zhang, Q.; Xie, J.; Lee, J. Y.; Zhang, J.; Boothroyd, C. Synthesis of Ag@AgAu Metal Core/Alloy Shell Bimetallic Nanoparticles with Tunable Shell Compositions by a Galvanic Replacement Reaction. *Small* **2008**, *4*, 1067−1071.
(27) Goodman, A. M.; Cao, Y.; Urban, C.; Neumann, O.; Ayala-Orozco, C.; Knight, M. W.; Joshi, A.; Nordlande, P.; Halas, N. J. The Surprising in Vivo Instability of Near-IR-Absorbing Hollow Au-Ag Nanoshells. *ACS Nano* **2014**, *8*, 3222−3231.
(28) Shahjamali, M. M.; Bosman, M.; Cao, S.; Huang, X.; Saadat, S.; Martinsson, E.; Aili, D.; Tay, Y. Y.; Liedberg, B.; Loo, S. C. J.; Zhang, H.; Boey, F.; Xue, C. Gold Coating of Silver Nanoprisms. *Adv. Funct. Mater.* **2012**, *22*, 849−854.
(29) Zhao, L.; Ding, K.; Ji, X.; Li, J.; Wang, H.; Yang, W. Formation of Hollow Ag/Au Nanostructures in Seeding Approach: The Competition of Hydroxyl Groups with Chloride ions to Ag^{+}. *Colloids Surf., A* **2011**, *386*, 172−178.
(30) Jin, Y.; Dong, S. One-Pot Synthesis and Characterization of Novel Silver-Gold Bimetallic Nanostructures with Hollow Interiors and Bearing Nanospikes. *J. Phys. Chem. B* **2003**, *107*, 12902−12905.
(31) Métraux, G. S.; Cao, Y. C.; Jin, R.; Mirkin, C. A. Triangular Nanoframes Made of Gold and Silver. *Nano Lett.* **2003**, *35*, 519−522.
(32) Perrault, S. D.; Chan, W. C. W. Synthesis and Surface Modification of Highly Monodispersed, Spherical Gold Nanoparticles of 50−200 nm. *J. Am. Chem. Soc.* **2009**, *131*, 17042−17043.
(33) Gentry, S. T.; Fredericks, S. J.; Krchnavek, R. Controlled Particle Growth of Silver Sols through the Use of Hydroquinone as a Selective Reducing Agent. *Langmuir* **2009**, *25*, 2613−2621.
(34) Lee, Y.; Park, T. G. Facile Fabrication of Branched Gold Nanoparticles by Reductive Hydroxyphenol Derivatives. *Langmuir* **2011**, *27*, 2965−2971.
(35) Li, J.; Han, J.; Xu, T.; Guo, C.; Bu, X.; Zhang, H.; Wang, L.; Sun, H.; Yang, B. Coating Urchin-like Gold Nanoparticles with Polypyrrole Thin Shells To Produce Photothermal Agents with High Stability and Photothermal Transduction Efficiency. *Langmuir* **2013**, *29*, 7102−7110.
(36) Shan, J.; Tenhu, H. Recent Advances in Polymer Protected Gold Nanoparticles: Synthesis, Properties, and Applications. *Chem. Commun.* **2007**, *44*, 4580−4598.
(37) Wong, Y. J.; Zhu, L.; Teo, W. S.; Tan, Y. W.; Yang, Y.; Wang, C.; Chen, H. Revisiting the Stöber Method: Inhomogeneity in Silica Shells. *J. Am. Chem. Soc.* **2011**, *133*, 11422−11425.
(38) Yang, J.; Shen, D.; Zhou, L.; Li, W.; Li, X.; Yao, C.; Wang, R.; El-Toni, A. M.; Zhang, F.; Zhao, D. Spatially Confined Fabrication of Core-Shell Gold Nanocages@Mesoporous Silica for Near-Infrared Controlled Photothermal Drug Release. *Chem. Mater.* **2013**, *25*, 3030−3037.
(39) Zhang, X.; Xu, X.; Li, T.; Lin, M.; Lin, X.; Zhang, H.; Sun, H.; Yang, B. Composite Photothermal Platform of Polypyrrole-Enveloped Fe_3O_4 Nanoparticle Self-Assembled Superstructures. *ACS Appl. Mater. Interfaces* **2014**, *6*, 14552−14561.
(40) Ye, Q.; Zhou, F.; Liu, W. Bioinspired Catecholic Chemistry for Surface Modification. *Chem. Soc. Rev.* **2011**, *40*, 4244−4258.
(41) Lin, L.-S.; Cong, Z.-X.; Cao, J.-B.; Ke, K.-M.; Peng, Q.-L.; Gao, J.-H.; Yang, H.-H.; Liu, G.; Chen, Xi. Multifunctional Fe_3O_4@ Polydopamine Core-Shell Nanocomposites for Intracellular mRNA Detection and Imaging-Guided Photothermal Therapy. *ACS Nano* **2014**, *8*, 3876−3883.
(42) Park, J.; Brust, T. F.; Lee, H. J.; Lee, S. C.; Watts, V. J.; Yeo, Y. Polydopamine-Based Simple and Versatile Surface Modification of Polymeric Nano Drug Carriers. *ACS Nano* **2014**, *8*, 3347−3356.
(43) Liu, Y.; Ai, K.; Lu, L. Polydopamine and Its Derivative Materials: Synthesis and Promising Applications in Energy, Environmental, and Biomedical Fields. *Chem. Rev.* **2014**, *114*, 5057−5115.
(44) Black, K. C.; Yi, J.; Rivera, J. G.; Zelasko-Leon, D. C.; Messersmith, P. B. Polydopamine-Enabled Surface Functionalization of Gold Nanorods for Cancer Cell-Targeted Imaging and Photothermal Therapy. *Nanomedicine* **2013**, *8*, 17−28.
(45) Liu, R.; Guo, Y.; Odusote, G.; Qu, F.; Priestley, R. D. Core−Shell Fe_3O_4 Polydopamine Nanoparticles Serve Multipurpose as Drug Carrier, Catalyst Support and Carbon Adsorbent. *ACS Appl. Mater. Interfaces* **2013**, *5*, 9167−9171.
(46) Chen, T.; Shao, M.; Xu, H.; Zhuo, S.; Liua, S.; Lee, S.-T. Molecularly Imprinted Polymer-Coated Silicon Nanowires for Protein Specific Recognition and Fast Separation. *J. Mater. Chem.* **2012**, *22*, 3990−3996.
(47) Lee, H.; Dellatore, S. M.; Miller, W. M.; Messersmith, P. B. Mussel-Inspired Surface Chemistry for Multifunctional Coatings. *Science* **2007**, *318*, 426−430.

DOI: 10.1021/acsami.5b02666
ACS Appl. Mater. Interfaces 2015, 7, 11613−11623

(48) Zhou, J.; Duan, B.; Fang, Z.; Song, J.; Wang, C.; Messersmith, P. B.; Duan, H. Interfacial Assembly of Mussel-Inspired Au@Ag@ Polydopamine Core−Shell Nanoparticles for Recyclable Nanocatalysts. *Adv. Mater.* **2014**, *26*, 701−705.
(49) Liu, Y.; Ai, K.; Liu, J.; Deng, M.; He, Y.; Lu, L. Dopamine-Melanin Colloidal Nanospheres: An Efficient Near-Infrared Photothermal Therapeutic Agent for in Vivo Cancer Therapy. *Adv. Mater.* **2013**, *25*, 1353−1359.
(50) Liu, X.; Cao, J.; Li, H.; Li, J.; Jin, Q.; Ren, K.; Ji, J. Mussel-Inspired Polydopamine: A Biocompatible and Ultrastable Coating for Nanoparticles in Vivo. *ACS Nano* **2013**, *7*, 9384−9395.
(51) Wiley, B.; Sun, Y.; Mayers, B.; Xia, Y. Shape-Controlled Synthesis of Metal Nanostructures: The Case of Silver. *Chem.—Eur. J.* **2005**, *11*, 454−463.
(52) Hong, S.; Na, Y. S.; Choi, S.; Song, I. T.; Kim, W. Y.; Lee, H. Non-Covalent Self-Assembly and Covalent Polymerization Co-Contribute to Polydopamine Formation. *Adv. Funct. Mater.* **2012**, *22*, 4711−4717.
(53) d'Ischia, M.; Napolitano, A.; Pezzella, A.; Meredith, P.; Sarna, T. Chemical and Structural Diversity in Eumelanins: Unexplored Bio-Optoelectronic Materials. *Angew. Chem., Int. Ed.* **2009**, *48*, 3914−3921.
(54) Simon, J. D.; Peles, D. N. The Red and the Black. *Acc. Chem. Res.* **2010**, *43*, 1452−1460.
(55) Yang, Y.; Guo, M. Preparation of Fluorescent SiO_2 Particles with Single CdTe Nanocrystal Cores by the Reverse Microemulsion Method. *Adv. Mater.* **2005**, *17*, 2354−2357.
(56) Ghosh, S. K.; Pal, T. Interparticle Coupling Effect on the Surface Plasmon Resonance of Gold Nanoparticles: From Theory to Applications. *Chem. Rev.* **2007**, *107*, 4797−4862.
(57) Stewart, M. E.; Anderton, C. R.; Thompson, L. B.; Maria, J.; Gray, S. K.; Rogers, J. A.; Nuzzo, R. G. Nanostructured Plasmonic Sensors. *Chem. Rev.* **2008**, *108*, 494−521.
(58) Nehl, C. L.; Liao, H.; Hafner, J. H. Optical Properties of Star-Shaped Gold Nanoparticles. *Nano Lett.* **2006**, *6*, 683−688.
(59) Chen, H.-T.; Padilla, W. J.; Cich, M. J.; Azad, A. K.; Averitt, R. D.; Taylor, A. J. A Metamaterial Solid-State Terahertz Phase Modulator. *Nat. Photonics* **2009**, *3*, 148−151.
(60) Contreras-Cáceres, R.; Sánchez-Iglesias, A.; Karg, M.; Pastoriza-Santos, I.; Pérez-Juste, J.; Pacifico, J.; Hellweg, T.; Fernández-Barbero, A.; Liz-Marzán, L. M. Encapsulation and Growth of Gold Nanoparticles in Thermoresponsive Microgels. *Adv. Mater.* **2008**, *20*, 1666−1670.
(61) Lim, D.; Barhoumi, A.; Wylie, R. G.; Reznor, G.; Langer, R. S.; Kohane, D. S. Enhanced Photothermal Effect of Plasmonic Nanoparticles Coated with Reduced Graphene Oxide. *Nano Lett.* **2013**, *13*, 4075−4079.
(62) Jian, N.; Shao, L.; Wang, J. (Gold Nanorod Core)/(Polyaniline Shell) Plasmonic Switches with Large Plasmon Shifts and Modulation Depths. *Adv. Mater.* **2014**, *26*, 3282−3289.
(63) Tian, L.; Chen, E.; Gandra, N.; Abbas, A.; Singamaneni, S. Gold Nanorods as Plasmonic Nanotransducers: Distance-Dependent Refractive Index Sensitivity. *Langmuir* **2012**, *28*, 17435−17442.
(64) Chen, H.; Kou, X.; Yang, Z.; Ni, W.; Wang, J. Shape- and Size-Dependent Refractive Index Sensitivity of Gold Nanoparticles. *Langmuir* **2008**, *24*, 5233−5237.
(65) Roper, D. K.; Ahn, W.; Hoepfner, M. Microscale Heat Transfer Transduced by Surface Plasmon Resonant Gold Nanoparticles. *J. Phys. Chem. C* **2007**, *111*, 3636−3641.
(66) Tian, Q. W.; Jiang, F. R.; Zou, R. J.; Liu, Q.; Chen, Z. G.; Zhu, M. F.; Yang, S. P.; Wang, J. L.; Wang, J. H.; Hu, J. Q. Hydrophilic Cu_9S_5 Nanocrystals: A Photothermal Agent with a 25.7% Heat Conversion Efficiency for Photothermal Ablation of Cancer Cells in Vivo. *ACS Nano* **2011**, *5*, 9761−9771.
(67) Hessel, C. M.; Pattani, V. P.; Rasch, M.; Panthani, M. G.; Koo, B.; Tunnell, J. W.; Korgel, B. A. Copper Selenide Nanocrystals for Photothermal Therapy. *Nano Lett.* **2011**, *11*, 2560−2566.
(68) Hilgenbrink, A. R.; Low, P. S. Folate Receptor-Mediated Drug Targeting: From Therapeutics to Diagnostics. *J. Pharm. Sci.* **2005**, *94*, 2135−2146.
(69) Qin, X. C.; Guo, Z. Y.; Liu, Z. M.; Zhang, W.; Wan, M. M.; Yang, B. W. Folic Acid-Conjugated Graphene Oxide for Cancer Targeted Chemo-Photothermal Therapy. *J. Photochem. Photobiol., B* **2013**, *120*, 156−162.

DOI: 10.1021/acsami.5b02666
ACS Appl. Mater. Interfaces 2015, 7, 11613−11623